Transient two-dimensional spectroscopy with linear absorption corrections applied to temperature-jump two-dimensional infrared

Transient two-dimensional spectroscopy with linear absorption corrections applied to temperature-jump two-dimensional infrared

Kevin C. Jones, Ziad Ganim, Chunte Sam Peng, and Andrei Tokmakoff*

Department of Chemistry, Massachusetts Institute of Technology, 77 Massachusetts Avenue, 6-213, Cambridge, Massachusetts 02139, USA
**Corresponding author: tokmakof@mit.edu*

Received September 22, 2011; accepted October 14, 2011;
posted October 20, 2011 (Doc. ID 155108); published December 9, 2011

Multidimensional spectroscopies provide increased spectral information but time resolution is often limited by the picosecond lifetimes of the transitions they probe. At the expense of additional complexity, *transient* multidimensional techniques extend the accessible timescales for studying nonequilibrium chemical and biophysical phenomena. Transient temperature-jump (T-jump) experiments are particularly versatile, since they can be applied to any temperature-dependent change of state. We have developed a method to correct transient nonlinear techniques for distortions resulting from transient linear absorption of the probing pulses, distortions which can lead to false interpretations of the data. We apply these corrections in the collection of T-jump transient two-dimensional infrared spectra for the peptides diglycine and the β-hairpin peptide trpzip2. For diglycine, the T-jump induces changes in H-bonding, a response which is inherent to all aqueous systems. The trpzip2 results probe the hairpin unfolding kinetics and reveal two time scales: <10 ns increased flexibility and 1.1 μs β-hairpin disordering.

OCIS codes: 300.6420, 120.6200, 300.6500, 300.6340, 320.7150, 300.6290.

1. INTRODUCTION

Multidimensional spectroscopies such as two-dimensional infrared (2D IR) and 2D electronic spectroscopy are becoming increasingly important for the study of structure [1,2], dynamics [3,4], and reactions [5] in the condensed phase, from solutions [6] to biological systems [7–9]. Multidimensional techniques are advantageous because they have femtosecond time resolution, spectral information is spread over multiple frequency axes, peak intensities scale to high order with the dipole, and cross peaks reveal both coupling and dipole orientation [10]. The use of multiple pulses also allows for time-dependent experiments in which transitions are tagged and then probed after a variable waiting time [11]. These waiting time experiments have been applied to study many problems including hydrogen-bond switching in water [3], photosynthetic energy transfer [9], protein conformational dynamics [12,13], and the chemical exchange of small molecule complexes in solution [6,14]. Although waiting time experiments are well suited to studying ultrafast timescales, their effective time window is limited by the vibrational or electronic lifetime of the chromophore—picoseconds in the case of condensed phase vibrations.

To overcome the lifetime-limited accessible time window of waiting time experiments, transient multidimensional experiments have been introduced in which spectra of a nonequilibrium system are collected following a triggering event [15]. For example, 2D IR has been used to track processes triggered by ultrafast or nanosecond temperature-jump (T-jump) laser pulses [16], such as for the study of photoswitchable peptide conformational changes [15,17], ligand release [18,19], charge injection [20], and protein folding [21–23]. For these experiments, the accessible temporal window is not defined by spectroscopic relaxation properties of the oscillator, but rather by the time scale of the initiated process and the return to equilibrium. These transient 2D IR experiments are often done in conjunction with nonlinear experiments in one frequency dimension, such as dispersed pump probe (DPP), dispersed vibrational echo (DVE) [24,25], or heterodyned-detected dispersed vibrational echo (HDVE), which are related to the real component, the power spectrum, and complex component, respectively, of the projection of the 2D IR spectrum onto the ω_3 axis [26]. These one-dimensional (1D) experiments provide a reduced version of the 2D IR information, but they can be collected more quickly and easily to provide better sampling of transient events.

The addition of a triggering pulse to a third-order nonlinear experiment increases the complexity of data collection and interpretation. Formally, transient multidimensional laser triggered experiments are fifth-order nonlinear experiments and they require a high signal-to-noise ratio to identify differences between the transient and equilibrium spectra, often necessitating dual frequency modulation strategies for double differential signal detection. Data collection is often slowed down to the repetition rate of the triggering event rather than the probing laser rate. Also, linear transient refractive index and absorption effects induced by the triggering pulse can lead to spurious peaks that overshadow the molecular changes of interest [27]. These pulse propagation distortions are particularly problematic for solutes and solvents whose absorbance in the probing frequency range changes significantly in response to the triggering event. For example, in the T-jump triggered transient 2D IR (t-2D IR) studies described in this paper, the D_2O solvent linear absorbance is dependent on the temperature. Thus, the interrogating IR pulses and signal are

shaped by the time-dependent temperature relaxation of the solvent. Although in this case the timescales are not expected to be significantly affected by the linear absorption, spurious peaks may alter the molecular interpretation. After overcoming the technical challenges, interpreting transient data is difficult due to the congested nature of the spectra, which have overlapping and interfering positive and negative peaks. Loss and gain features in the transient spectrum can show up as both positive and negative changes. Therefore, reducing spectral complexity by correcting for uninformative linear effects greatly aids the data analysis.

T-jump experiments have been used extensively in studies of protein and peptide folding kinetics, often by probing changes in the structurally sensitive amide I IR vibrational absorption spectrum. Relative to continuous-wave linear absorption T-jump techniques, the multidimensional T-jump amide I experiment is often challenged by greater noise, longer acquisition times, and technical complexity, but it offers enhanced spectral content, background free signals, and ultrafast time resolution. T-jump amide I IR experiments have almost exclusively measured linear absorption changes using techniques such as step-scan Fourier transform infrared (FTIR) [28], single wavelength, continuous-wave IR lasers [29–31], or ultrafast IR pulse absorption [32]. The first two are limited to the time resolution of the IR detector and all three require additionally collecting the transient spectra of the solvent to isolate the solute response. The major advantage of the multidimensional T-jump amide I experiment is increased spectral content, allowing for further disentanglement of the crowded amide I spectrum and simultaneous monitoring of crosspeaks which indicate coupling between vibrations. Although our T-jump t-2D IR experiment's time resolution is limited by the nanosecond pulse length of the T-jump laser, the method is fundamentally limited only by the picosecond time scale for vibrational relaxation in water. Also, since the nonlinear signal from the solvent is usually negligible, only data on one sample needs to be collected. All laser-induced T-jump experiments are limited by cavitation, thermal lensing, and beam homogeneity.

In a previous publication, we presented the design, construction, and testing of a transient 2D IR spectrometer for use in T-jump measurements [22]. In this paper, we describe data acquisition methods that correct for nonequilibrium absorption and dispersion effects in T-jump t-2D IR spectroscopy to isolate the desired kinetics for chemical processes. We first apply these methods to the model dipeptide diglycine to measure the relaxation of a small molecule which should not exhibit a response in the nanosecond–millisecond window of our T-jump. We then collect the t-2D IR spectra of the peptide trpzip2 (TZ2) to interpret the disordering kinetics of an extensively studied fast folding β-hairpin. Although the techniques are used to study the amide I vibrations of peptides through nonlinear T-jump experiments, the topics discussed are generalizable for any temperature-dependent equilibrium or transient multidimensional spectroscopy.

2. EXPERIMENTAL

A. Mid-Infrared Spectroscopy

All infrared probing methods reported are heterodyne-detected ultrafast third-order nonlinear spectroscopies performed in the boxcar geometry and detected using spectral interferometry with an external local oscillator (LO) pulse. Nonlinear infrared spectra were collected at 1 kHz using 90 fs pulses centered at ~1650 cm^{-1} (6 μm) with 160 cm^{-1} FWHM bandwidth as described previously [10]. The experimental layout of the sample and detection compartments is shown in Fig. 1. Three pulses (E_1, E_2, and E_3), separated by sequential time intervals τ_1 and τ_2 were focused into the sample to a ~75 μm diameter spot to generate a nonlinear signal field E_{sig}. The LO was focused through the same sample volume as the other infrared beams, but it was delayed ~60 ps relative to E_3. This delay is long enough not to interfere with the IR signal generation but short enough that all IR fields experience the same perturbations. The LO and signal were spatially overlapped by combining them on opposite sides of a beamsplitter. The signal field was detected using balanced detection of the two resulting heterodyned signals, which have a relative 180° phase shift. After diffracting the two resulting beams off of a 40 lines/mm grating in a 190 mm spectrograph (Triax 190, Jobin Yvon), interference between E_{sig} and E_{LO} was detected with ~4.7 cm^{-1} resolution on a 2×64 element mercury cadmium telluride array (IR-0144, Infrared Systems Development). Beam 2 or 3 was mechanically chopped at 500 Hz to remove scatter and the LO spectrum. LO timing and phasing were achieved by comparison to a two beam DPP spectrum. The resulting detection frequency axis is referred to as ω_3. Both HDVE and 2D IR spectra were collected with all parallel polarization (ZZZZ) and at $\tau_2 = 150$ fs to minimize nonresonant signal from the CaF_2 windows.

B. Temperature-Jump

The T-jump laser system and its synchronization with the mid-IR system have been described previously [22]. Briefly, the

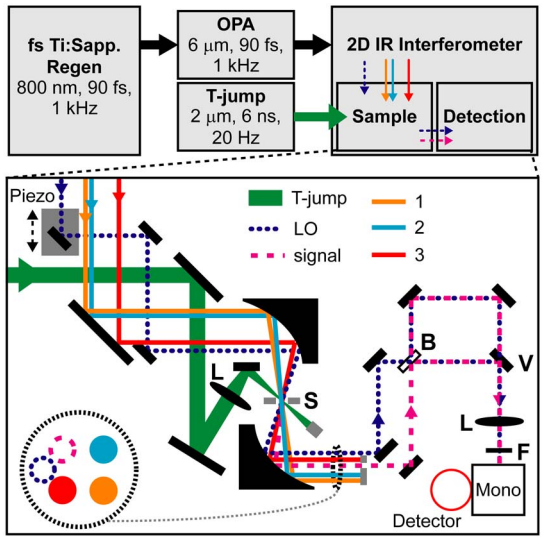

Fig. 1. (Color online) The output of a femtosecond Ti:sapphire regenerative amplifier is converted to the IR by difference frequency generation in an optical parametric amplifier and split into four IR beams in the 2D IR interferometer. Inlay: Three IR beams generate IR third-order signal at the sample. The T-jump laser is overlapped spatially with the IR beams at the sample and delayed in time electronically. The LO beam is overlapped spatially with the IR beams at the sample, but delayed from the other IR pulses. The signal and LO beams are overlapped spatially and temporally at the detector and detected using balanced detection. The LO beam's delay can be stepped using the piezo-controlled stage for PMSI or FTSI measurements. L: lens, S: sample, B: beam-splitter, V: vertically displaced mirror, F: low pass $\lambda = 3.4\,\mu$m filter.

6 ns, 1.98 μm, 9 mJ T- pulse was generated at 20 Hz through the combination of a *Q*-switched Nd:YAG (yttrium aluminum garnet) laser and a β-barium borate based optical parametric oscillator (YG981c, OPOTEK) tuned to match the $\nu = 2 \leftarrow 0$ O-D stretch of D_2O. The T-jump laser is focused to a 500 μm waist at the same point in the sample as the mid-IR beams, creating a 10–12 °C jump in our sample in <10 ns. Since the T-jump focus is approximately five times the size of the mid-IR waist, the T-jump in the region of mid-IR beam overlap is uniform. The electronic delay generator creates the time-delay between the T-jump pulse and the first of the 50 mid-IR beam sets with an instrument response time of 6 ns and a delay range of nanoseconds–milliseconds. In addition to electrical isolation, we found it necessary to acoustically isolate the T-jump laser from the IR laser table to remove interferometrically-measurable noise created by flashlamp firing.

The difference between repetition rates resulted in a 50 ms window with 50 collected mid-IR spectra between each T-jump shot. Figure 2 shows the time delays between the 1 kHz IR and 20 Hz T-jump pulses. We denote the time-delay between the T-jump pulse and the *j*th mid-IR pulse following the T-jump as

$$\tau^j = \tau + j \times (1\,\text{ms}), \quad \text{for } j = 0, 1, 2, \ldots, 49. \tag{1}$$

τ is the primary time-delay between the T-jump pulse and the 2D IR probe event following it. The T-jump pulse was spatially and temporally overlapped with the mid-IR pulse by monitoring the transmittance of the LO through the transiently heated solvent. Zero time, $\tau^0 = 0$, was set at the delay when the transient transmittance signal of the LO was half of the maximum transient transmission, which was a ~5% increase over equilibrium. The T-jump re-equilibrates by thermal diffusion into the sample cell windows, reaching half its initial value at $t \sim$ 1.5 ms and the time-trace can be described by a stretched exponential of the form $\exp[-(t/\tau_s)^\beta]$ where $\tau_s = 2.05$ ms and $\beta = 0.67$.

Transient data collection is complicated by chopping to remove the homodyned LO term of the collected signal. To collect the complementary 500 Hz chopped and unchopped mid-IR spectra at a given T-jump delay τ^i, the phase of the chopper was modulated between 0° and 180°. At a phase of 0° (180°), the odd (even) mid-IR pulses following the T-jump pulse are open, while the even (odd) pulses are blocked.

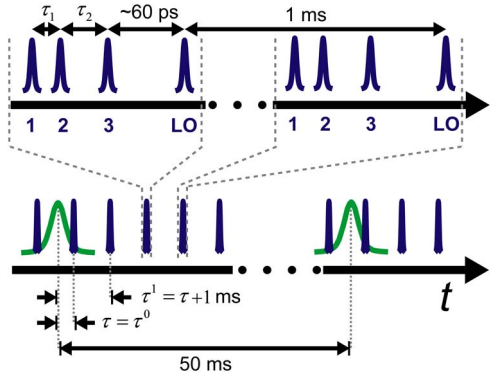

Fig. 2. (Color online) IR beams (blue) 1,2 and 2,3 are delayed by τ_1 and τ_2. The LO reaches the sample ~60 ps after beam 3. The original IR pulse, from which beams 1,2,3 and LO are created, is generated at 1 kHz, which creates a 1 ms lag between sets of IR pulses. The 20 Hz T-jump pulse (green) is delayed electronically relative to the IR pulses. The first IR pulse set following the T-jump pulse arrives at a delay of $\tau = \tau^0$. The next 49 IR pulse sets arrive at $\tau^j = \tau + j \times (1\,\text{ms})$.

C. Sample Preparation

The tryptophan zipper β-hairpin peptide, TZ2 (NH_2-SWTWENGKWTWK-$CONH_2$) was synthesized as described previously [33]. The TZ2 samples were dissolved in pH 2.5 DCl in D_2O solvent to 10 mg/mL concentrations [optical density (OD) of ~0.05]. Diglycine (L-glycyl-L-glycine) was purchased from Sigma and dissolved in D_2O (pH = 6.5) to a concentration of 20 mg/mL (OD of ~0.9) unless noted otherwise. ~25 μL peptide solution was sandwiched between two 1 mm thick CaF_2 windows with a 50 μm pathlength defined by a teflon spacer. The TZ2 sample was then sealed in a brass cell held at $T_0 = 35$ °C by a regulated water bath ($T_0 = 20$ °C for diglycine). For these samples, any changes induced by the T-jump relax reversibly back to equilibrium within the 50 ms window and flowing the sample was found to be unnecessary in this case.

3. TRANSIENT DATA COLLECTION AND PROCESSING

A. Theoretical Background

The purpose of our data acquisition process is to perform transient nonlinear spectroscopy in the absence of distortions or artifacts that may arise from propagation through the nonequilibrium environment prepared by the trigger pulse. As the mid-IR laser pulses pass through the sample, their group velocity is affected by the temperature-dependent (T-jump delay-dependent) real part of the refractive index, $n(\omega; \tau^j)$, and their magnitude is affected by temperature-dependent absorption, $\kappa(\omega; \tau^j)$. The complex refractive index experienced by the mid-IR pulses is given by

$$\tilde{n}(\omega; \tau^j) = n(\omega; \tau^j) + i\kappa(\omega; \tau^j). \tag{2}$$

We write this noting that this is not the equilibrium index of refraction, but an effective index that reflects an average over the dielectric response of the sample, $\varepsilon(\omega)$, following the T-jump for frequencies $\omega > 2\pi/\tau^i$. As with other transient experiments, it will include changes in absorption and dispersion that arise from molecular dynamics on time scales faster than the T-jump delay, including acoustic and thermal responses.

The real, time-domain electric field of one of the incident pulses after passing through the sample, $E_\alpha(t; \tau^j)$, can be Fourier transformed (FT) into the frequency domain to give the complex field,

$$\tilde{E}_\alpha(\omega; \tau^j) = e_\alpha(\omega) \exp[i\phi_\alpha(\omega)] \exp[i\tilde{n}(\omega; \tau^j)\omega l/c], \quad \alpha = 1, 2, 3, \text{LO}, \tag{3}$$

where e is the amplitude, ϕ is the phase, and the last term accounts for the temperature-dependent and T-jump delay-dependent linear refractive index change that accumulates as the field passes through the sample with path length l. c is the speed of light. Because beams 1, 2, 3, and the LO generate or interfere with the nonlinear signal, the linear $\tilde{n}$ propagation effects manifest themselves in the resulting nonlinear spectrum.

To remove the relative effect of the $n(\omega;\tau^j)$, the LO is aligned through the sample along with the other pulses. As a result, the group velocity of each beam increases by the same amount, minimizing the phase difference between them. Although the LO and signal are intentionally delayed relative to each other at the sample, the ~60 ps difference is negligible compared to the nanosecond T-jump pulse length. We therefore assume that the LO and signal are equally affected by the sample's linear refractive index as they pass through the sample.

Assessing how $\kappa(\omega;\tau^j)$ distorts the experimentally-measured nonlinear signal relative to an ideal (infinitely thin) sample signal requires a description of how absorption of each laser pulse affects the generated signal, which, in turn, is also affected by propagation through the sample [34–36]. The real time-domain signal electric field $E_{\mathrm{sig}}(t_3;\tau_1,\tau_2 = 150\,\mathrm{fs},\tau^j)$ results from the polarization induced in the sample by the time-delayed beams 1, 2, and 3, which is generated gradually as the pulses propagate through the sample. To a first approximation, the *combined* absorption of beams 1 and 2 imprints a depletion term $K(\omega_1;\tau^j)$ along the ω_1 axis [36] of the frequency domain 2D spectrum where

$$K(\omega_n;\tau^j) = \frac{1-\exp[-2\kappa(\omega_n;\tau^j)\omega_n l/c]}{2\kappa(\omega_n;\tau^j)\omega_n l/c}. \tag{4}$$

The combined depletion effect of beam 3 and the signal is expressed by $\exp[-\kappa(\omega_3;\tau^j)\omega_3 l/c]$. This conventional absorption term can be explained in terms of a transient grating picture in which the signal is generated by diffraction of beam 3 off of an E_1+E_2 generated grating or in the picture in which the absorption accumulated by beam 3 is imprinted on the signal that is gradually generated in the sample. The LO can be treated independently as a pulse that accumulates an $\exp[-\kappa(\omega_3;\tau^j)\omega_3 l/c]$ absorption term, as is shown in Eq. (3).

To a first approximation, absorbance of beams 1 and 2 distorts the resulting 2D spectrum along the ω_1 axis, whereas absorption of beam 3, the signal, and the LO affects ω_3. Since the LO experiences the same index as the remaining beams, the effect of $n(\omega;\tau^j)$ vanishes upon detection. Collecting the above terms, which assume the sample is a weak absorber and ignore coherent energy transfer during τ_1 and τ_3, we can approximate the effects of linear absorption as [36]:

$$\tilde{S}^{1,3}(\omega_1,\omega_3;\tau_2,\tau^j) \approx \tilde{S}(\omega_1,\omega_3;\tau_2,\tau^j)\times K(\omega_1;\tau^j) \times \exp[-2\kappa(\omega_3;\tau^j)\omega_3 l/c]. \tag{5}$$

Here, $\tilde{S}^{1,3}$ is the directly detected 2D spectrum where the superscripts 1 and 3 indicate the existence of distortions along ω_1 and ω_3. $\tilde{S}$ without superscripts is the desired spectrum that would be measured for an optically thin sample unaffected by linear propagation effects, but still shaped by the finite-bandwidth of our pulses, which acts to weaken apparent intensity on the wings of the spectrum. For the present work, τ_2 is always 150 fs and it is not explicitly shown in the rest of the equations in the paper for simplicity. The second term on the right in Eq. (5) represents the *combined* absorption of E_1/E_2, while the third term accounts for the absorption of $E_{\mathrm{LO}}+E_3/E_{\mathrm{sig}}$, which results in the factor of two. With negligible absorption, both correction terms approach one.

With propagation effects accounted for, we can properly define the signal electric field emerging from the sample. $\tilde{E}_{\mathrm{sig}}$ depends parametrically on τ_2, τ_1, and τ^j and can be expressed as

$$\tilde{E}^{1,3}_{\mathrm{sig}}(\omega_3;\tau_1,\tau^j) = e^1_{\mathrm{sig}}(\omega_3;\tau_1,\tau^j)\exp[i\phi_{\mathrm{sig}}(\omega_3;\tau_1,\tau^j)] \times \exp[i\tilde{n}(\omega_3;\tau^j)\omega_3 l/c]. \tag{6}$$

As above, the superscripts 1 and 3 indicate that the spectrum is distorted by propagation effects along the ω_1 and ω_3 axes. The $\tilde{E}_{\mathrm{LO}}$ T-jump delay dependence is solely due to the transient linear absorbance of the sample, whereas the signal amplitude and phase are also expected to change due to molecular dynamics during τ_1 and τ_2. Because propagation effects on the ω_1 axis cannot be cleanly expressed as a function of τ_1, the ω_1 distortion is folded into $e^1_{\mathrm{sig}}(\omega_3;\tau_1,\tau^j)$ while the ω_3 distortion is explicitly shown.

B. Data Collection

Our detector is a dual stripe array that collects data from 2×64 pixels at 1 kHz. The 1 kHz data is modulated by the electronically delayed 20 Hz T-jump laser and a 500 Hz chopper. The chopper phase is flipped periodically at ~0.1 Hz to fully characterize every combination of the 20 Hz and 500 Hz modulation. In practice, the detector measures intensity $I(\omega_3) = |\tilde{E}(\omega_3)|^2$ in the frequency domain after diffraction off of a grating. Characterization of $\tilde{E}$ requires interferometric detection. In both 2D IR and HDVE spectroscopy, $\tilde{E}_{\mathrm{sig}}$ was characterized by combining the signal and LO at a delay τ_{LO} and measuring the ω_3 difference spectrum of the LO with and without the signal present. In balanced detection, intensities are observed for the out-of-phase intensity from the upper (+) and lower (–) stripes. The spectrum of the LO (chopper blocked signal, °) is

$$I^{\circ}_{\pm}(\omega;\tau^j) = |\tilde{E}_{\mathrm{LO}}(\omega;\tau^j)|^2 = [e_{\mathrm{LO}}(\omega)]^2\exp[-2\kappa(\omega;\tau^j)\omega l/c] \tag{7}$$

and that of the combined E_{LO} and E_{sig} (chopper open) is

$$\begin{aligned} I^{1,3}_{\pm}(\omega_3;\tau_1,\tau^j,\tau_{\mathrm{LO}}) &= |\tilde{E}^{1,3}_{\mathrm{sig}}(\omega_3;\tau_1,\tau^j) \\ &\quad + \tilde{E}_{\mathrm{LO}}(\omega_3;\tau^j)\exp[-i\omega_3\tau_{\mathrm{LO}}]|^2 \\ &= \exp[-2\kappa(\omega_3;\tau^j)\omega_3 l/c]\times\{[e_{\mathrm{LO}}(\omega_3)]^2 \\ &\quad + [e^1_{\mathrm{sig}}(\omega_3;\tau_1,\tau^j)]^2 \pm 2e_{\mathrm{LO}}(\omega_3)e^1_{\mathrm{sig}}(\omega_3;\tau_1,\tau^j) \\ &\quad \times\cos[\Delta\phi(\omega_3;\tau_1,\tau^j)+\tau_{\mathrm{LO}}\omega_3]\}. \end{aligned} \tag{8}$$

Here we have defined

$$\Delta\phi(\omega_3;\tau_1,\tau^j) = \phi_{\mathrm{sig}}(\omega_3;\tau_1,\tau^j) - \phi_{\mathrm{LO}}(\omega_3). \tag{9}$$

By sending the LO through the sample, the shared change in real refractive index induced by the T-jump delays the signal, LO, and beams 1, 2, and 3 by the same relative amount and $n(\omega;\tau^j)$ drops out of Eq. (8) [22]. If the LO is not passed through the sample, the relative time-delay between the LO and other beams changes with the temperature and the resulting spectra are not phased properly, which results in the mixing of the real and imaginary parts.

If the interference cross-term in Eq. (8) (which is proportional to the desired nonlinear signal field) were Fourier transformed along τ_1, it would result in $\tilde{S}^{1,3}_{2D}$ given in Eq. (5). Instead, the cross-term in Eq. (8) is separated and the ω_3-axis linear

absorption distortion is directly removed using the following data acquisition steps:

$$S^1(\omega_3;\tau_1,\tau^j,\tau_{\mathrm{LO}}) = \left[\left\langle\frac{I_+^{1,3}-I_-^{1,3}}{I_+^{1,3}+I_-^{1,3}}\right\rangle - \left\langle\frac{I_+^{\circ}-I_-^{\circ}}{I_+^{\circ}+I_-^{\circ}}\right\rangle\right]\times[e_{\mathrm{LO}}(\omega_3)]^2. \tag{10}$$

$$= 2e_{\mathrm{LO}}(\omega_3)e^1_{\mathrm{sig}}(\omega_3;\tau_1,\tau^j)\cos[\Delta\phi(\omega_3;\tau_1,\tau^j)+\tau_{\mathrm{LO}}\omega_3]. \tag{11}$$

$$\approx S(\omega_3;\tau_1,\tau^j,\tau_{\mathrm{LO}})\times K(\omega_1;\tau^j). \tag{12}$$

The out-of-phase detection arrays are subtracted to remove the homodyne terms and divided by the sum. The denominator divides out the linear absorption term due to LO, signal, and beam 3 and normalizes the heterodyne signal for each single shot to remove shot-to-shot fluctuations before averaging. These operations are performed at 1 kHz and the data is then averaged, as indicated by triangular brackets. Finally, the subtracted, shot-normalized, and averaged chopped terms are subtracted. The resulting signal has been corrected for linear absorption along ω_3. The superscript 1 indicates that there are still distortions along ω_1. The $[e_{\mathrm{LO}}(\omega_3)]^2$ term, the IR pulse spectrum in the absence of the sample, is calculated using a separate FTIR absorbance spectrum collected at the equilibrium temperature and the T-relaxed $I_{\pm}^{\circ}(\omega;\tau^{\mathrm{ref}})$, where ref = 48 or 49 [Eq. (7)].

Theoretically, the second term on the right of Eq. (10) involving I° is not necessary assuming balanced detection, but we found it essential for removing scatter and electrical noise as well as for correcting for residual intensity mismatch between the stripes. To remove any small electrical noise that might show up in the denominator of the first term on the right of Eq. (10), a background was collected without any IR beams beforehand and subtracted directly from all the raw data. Data whose integrated LO intensity was less than a preset cutoff of ~50% of the average was rejected to remove errant shots.

Because of the difference in T-jump and mid-IR laser repetition rate, for each τ we actually collect 50 time delays, τ^j. Each of these 50 data sets are collected, saved, and processed independently and the last two spectra, $j = 48$ and 49, are assumed to be equilibrium spectra collected after the T-jump has relaxed back to the initial temperature.

C. Post Processing

To correct for the residual distortion in S^1 due to absorption of beams 1 and 2, the imaginary refractive index is calculated using the τ^j-dependent LO spectra. The differential absorption relative to the equilibrium LO was calculated and added to the reference absorption measured using an FTIR collected at the equilibrium temperature:

$$\kappa(\omega;\tau^j) = \Delta\kappa^{j,\mathrm{ref}}(\omega;\tau^j) + \kappa^{\mathrm{Eq}}_{\mathrm{FTIR}}(\omega), \tag{13}$$

$$= \frac{-c}{2\omega l}\ln\left[\frac{I_+^{\circ}(\omega;\tau^j)+I_-^{\circ}(\omega;\tau^j)}{I_+^{\circ}(\omega;\tau^{\mathrm{ref}})+I_-^{\circ}(\omega;\tau^{\mathrm{ref}})}\right] + \kappa^{\mathrm{Eq}}_{\mathrm{FTIR}}(\omega), \quad \begin{cases}\mathrm{ref}=48, & \text{for } j=0,2,\ldots,48\\ \mathrm{ref}=49, & \text{for } j=1,3,\ldots,49\end{cases}. \tag{14}$$

$\Delta\kappa^{j,\mathrm{ref}}(\omega;\tau^j)$ represents the relative change in linear absorption between the τ^j transient spectra and the reference spectrum, $I^{\circ}(\omega;\tau^{48})$ or $I^{\circ}(\omega;\tau^{49})$, which is analogous to measuring the linear absorption using $I(\tau^j)/I(\mathrm{ref})$. Ideally, the sample has returned to equilibrium or been replaced with a fresh equilibrium sample within 48 ms. $\kappa(\omega;\tau^j)$ takes into consideration the absorption due to the solvent, solute, and the CaF_2 windows. For the t-2D IR, the ω_1 correction is applied after the FT into ω_1:

$$\tilde{S}(\omega_1,\omega_3;\tau^j,\tau_{\mathrm{LO}}) \approx \tilde{S}^1(\omega_1,\omega_3;\tau^j,\tau_{\mathrm{LO}})\times[K(\omega_1;\tau^j)]^{-1}. \tag{15}$$

The correction in Eq. (15) removes the τ-dependent absorption due to beams 1 and 2.

For t-HDVE, we cannot directly apply a correction for ω_1 because we only have 1D ω_3-slices. Instead, we indirectly correct for ω_1-distortions by multiplying the correction along ω_3:

$$S(\omega_3;\tau_1,\tau^j,\tau_{\mathrm{LO}}) \approx S^1(\omega_3;\tau_1,\tau^j,\tau_{\mathrm{LO}})\times[K(\omega_3;\tau^j)]^{-1}. \tag{16}$$

Since this is formally only correct for diagonal peaks ($\omega_1 = \omega_3$) without spectral diffusion, this assumption is tenuous and should be applied cautiously.

The corrections along ω_1 and ω_3 described above approximately correct for linear absorbance of the finite-bandwidth pulses by the sample. Measuring the ideal 2D spectrum that would have been generated with infinite bandwidth pulses would require further manipulations to remove the effect of the limited spectral bandwidth of our pulses, which accentuates peaks near the middle of the pumping and probing spectra. Using the same approximations described above, to correct for this artificial intensity accentuation we would divide both the ω_1 and ω_3 axes by $[e_{\mathrm{LO}}(\omega)]^2$.

Once processed, averaged, and corrected, the data is presented as a difference signal in which the last two spectra are subtracted out as equilbrium spectra:

$$\Delta S(\tau^j) = S(\tau^j) - S(\tau^{\mathrm{ref}}), \qquad \begin{cases}\mathrm{ref}=48, & \text{for } j=0,2,\ldots,48\\ \mathrm{ref}=49, & \text{for } j=1,3,\ldots,49\end{cases}. \tag{17}$$

For 2D IR, $S(\tau^j)$ is either the real or absolute value t-2D IR signal after FT along τ_1: $S(\omega_1,\omega_3;\tau^j)$ and $|\tilde{S}(\omega_1,\omega_3;\tau^j)|$. For HDVE, $S(\tau^j)$ is either the real or absolute value HDVE signal at $\tau_1 = 0$ fs after exploiting the τ_{LO} dependence to calculate the complex signal: $S(\omega_3;\tau_2,\tau^j)$ and $|\tilde{S}(\omega_3;\tau_2,\tau^j)|$.

Although the methods described above were discussed specifically for transient T-jump 2D IR experiments, they are generalizable to temperature-dependent 2D IR studies or any heterodyne-detected transient third-order IR or electronic spectroscopy, particularly in cases where there is a strong linear transient absorbance response. For example, in studying protein folding problems, the linear absorbance of the D_2O solvent strongly depends on the temperature. Separating the temperature-dependent response of the protein requires correcting for the linear absorption distortions.

D. t-2D IR

For t-2D IR collection, τ_1 delays were undersampled in 14 fs steps scanned from 0 to >2.4 ps and to >1.3 ps for rephasing and nonrephasing surfaces, respectively, using delay stages (Aerotech, ANT-50L) with 100 nm reproducibility [22]. The τ_{LO} was set to 0. The data was collected in three nested 'for'

loops: (τ, τ_1, chopper phase). 7000 shots were collected at chopper = 0° before flipping to chopper = 180° and collecting another 7000 shots. The τ_1 delay was then stepped to the next delay and another 7000+7000 shots were collected. This stepping of τ_1 continued until the entire rephasing and nonrephasing surfaces were mapped out, at which point τ was changed and the process was repeated. Data was processed on the fly [Eq. (10)]; the τ_1 axis was then fast Fourier transformed after zero padding rephasing and nonrephasing interferograms to 16 ps and the undersampled data was reflected about the Nyquist frequency, $\omega_1 = 2\omega_{\text{Nyq.}} - \omega_1^{\text{FT}}$, where ω_1^{FT} is the frequency that results from direct FT [22]. The resulting spectrum was corrected along ω_1 [Eq. (15)] to give $\tilde{S}(\omega_1, \omega_3; \tau^j)$. Because all 50 of the τ-set spectra are collected with the same delay stage positions, the phasing correction is determined for the reference spectrum and then applied to the rest. Multiple spectra collected at the same τ are averaged in the frequency domain after correcting for the phasing error.

At each τ, a set of 50 2D IR spectra was collected in ~1.25 hours or 1.5 minutes per τ^j 2D IR spectrum. The τ spectra presented here for TZ2 (diglycine) are the result of ≥8(1) averages. Spectra with $\tau^j \geq 1$ ms but different τ were averaged together if the difference in time-delay was ≤1 μs. For example, the presented 1 ms T-jump delay spectra are the average of τ^1 spectra ranging from $\tau^1 = 10\,\text{ns} + 1\,\text{ms}$ to $\tau^1 = 1\,\mu\text{s} + 1\,\text{ms}$.

E. t-HDVE

For t-HDVE collection, the τ_1 delay was fixed to 0 and the τ_{LO} was stepped from 0 to 25 fs in 5 fs steps so that the complex spectrum could be calculated during data processing. The stepping was done using a piezo stage (THORLABS, NF5DP20S) for its 10 nm repeatability. The data was collected in three nested 'for' loops: (τ,τ_{LO}, chopper phase). 10 000 shots were collected at chopper = 0° before flipping to chopper = 180° and collecting another 10 000 shots. The τ_{LO} was then stepped by 5.0 fs, for which the carrier phase shift $\omega \times \Delta\tau_{\text{LO}} = \pi/2$ and another 10 000+10 000 shots were collected. Once all the τ_{LO} delays were collected, τ was changed and the process was repeated. Data was processed on the fly [Eq. (10)] and the resulting spectra were corrected for ω_1 distortions [Eq. (16)]. The complex HDVE signal, $\tilde{S}(\omega_3; \tau^j, \tau_{\text{LO}})$, was then calculated using either FT spectral interferometry (SI) or phase modulation SI, in which the difference and sum of τ_{LO}-stepped spectra were used to calculate the real and imaginary spectra followed by a phase correction back to $\tau_{\text{LO}} = 0$ [26]. The real HDVE signal $S(\omega_3; \tau^j, \tau_{\text{LO}})$ is equivalent to DPP, which is equal to the projection of the real 2D IR surface, $S(\omega_1, \omega_3; \tau^j)$, onto ω_3. The absolute value of the HDVE signal, $|\tilde{S}(\omega_3; \tau^j, \tau_{\text{LO}})|$, is equivalent to the square-root of the DVE [26].

Each τ set of 50 HDVE spectra was collected in ~2 minutes, or ~2.5 s per τ^j HDVE spectrum. The τ spectra presented here are the result of ≥6 averages. As with the 2D IR data, spectra with $\tau^j \geq 1$ ms but different τ were averaged together if the difference in time-delay was ≤1 μs.

4. RESULTS AND DISCUSSION

A. Diglycine

The dipeptide diglycine provides a baseline for the sorts of changes we should expect from a T-jump experiment on a peptide in which all dynamics are faster than the T-jump pulse and no conformational changes are observed in the nanosecond–millisecond T-jump window. We also study diglycine to compare the effects of correcting the nonlinear spectrum for linear absorption.

At the pH of 6.5 used here, diglycine exists in its zwitterionic form and shows two discernible peaks in the equilibrium 2D IR spectrum [Fig. 3(a)], a homogeneously broadened peak at 1595 cm^{-1} that is assigned to the antisymmetric stretch of the C-terminal carboxylate and an inhomogeneously broadened amide I' peak at 1674 cm^{-1}. Previous work on N-methylacetamide (NMA) has shown that the amide I' peak frequency strongly depends on the surrounding electrostatic environment defined by the multiple hydrogen-bond (H-bond) configurations to the backbone, as should the carboxylate [37]. Diglycine's amide I' peak is more inhomogeneous compared to NMA's peak, which suggests that there is a wider variety of H-bond configurations for diglycine as is expected given the proximity of the terminal H-bond-donating NH_3^+. These peaks are expected to blue shift with temperature as the average number of hydrogen bonds decrease.

B. Diglycine: Corrections for Linear Absorption

Linear absorption affects the nonlinear equilibrium spectrum by reducing intensity along both ω_1 and ω_3 wherever there is absorption in the FTIR. In order to compare the effects of linear absorption on the equilibrium spectrum of diglycine, different corrections were applied to the same raw data, as is shown in the columns of Fig. 3. The equilibrium spectra differ in the 1600 cm^{-1} region because the sample absorption (peak OD at $\omega = 1596\,\text{cm}^{-1}$ is 0.9) depletes intensity along ω_3, which results in an artificially large separation between the positive and negative peaks of the carboxylate stretch. This distortion also causes the ω_1 displacement between the positive and negative peak maxima observed in Fig. 3(a) for the amide I' vibration. Corrections along ω_3 and ω_1 [Figs. 3(c) and 3(e)] remove the distortions. The effect of ω_3-correction is larger than ω_1-correction, and both decrease the apparent anharmonicity.

Linear absorption in the transient spectra is more complicated than the equilibrium case because both the solvent and the solute respond to the T-jump. At our given initial temperature and T-jump size, the T-jump causes a ~5% increase in transmission due to the temperature dependency of the linear absorption, shown in Fig. 4(a). This ~5% transmission increase magnifies the underlying signal, which consists of the equilibrium spectrum and ~5% changes due to the T-jump. As a result, the difference spectra in Fig. 3(b) is due to two interfering spectral features: ~5% molecular changes resulting from the T-jump and ~5% magnified equilibrium spectrum due to the increased transmission. Most of the mixed-in equilibrium spectrum is removed by correction for beam 3, the LO, and the signal [Fig. 3(d)], where the τ-dependent ω_3-correction factor, $\exp[2\kappa(\omega; \tau^j)\omega l/c]$, is shown in Fig. 4(b). Full correction along both ω_1 and ω_3 reveals the undistorted difference spectrum [Fig. 3(f)], which differs from Fig. 3(d) primarily in the reweighting of features in the 1600 cm^{-1} region. Qualitatively, spurious spectral peaks like those seen in Figs. 3(b) and 3(d) can lead to false molecular interpretations. Figure 4(c) shows the ω_1-correction factor, $[K(\omega; \tau^j)]^{-1}$. Both the ω_3- and ω_1-correction factors have a significant contribution from the broad solvent HOD bend and the ω_1-correction factor is ~5x smaller than the ω_3-correction.

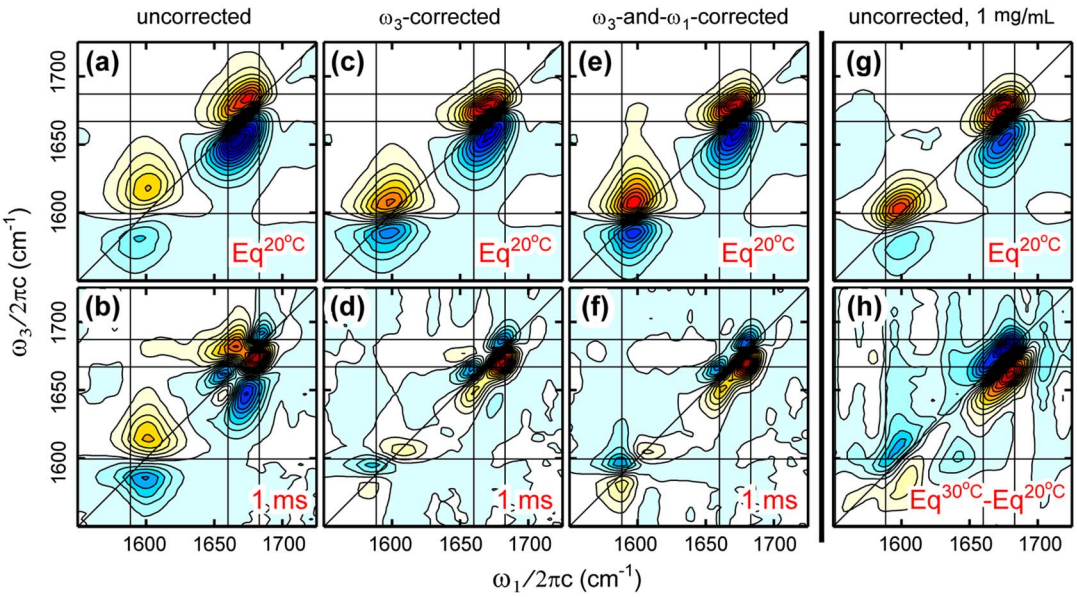

Fig. 3. (Color online) Absorptive (real) spectra of t-2D IR of diglycine are shown. Grid lines mark the three loss features shown in **f**. The first three columns (a-f) show data taken of 20 mg/mL diglycine (OD = 0.9) following a T-jump from 20 to 30 °C. The first row (a,c,e) shows equilibrium spectra at 20 °C. The second row (b,d,f) shows the 1 ms *difference* spectra. Columns 1–3 are calculated from the same data but with different corrections for linear absorption of the IR beams. Column 1 (a,b) is uncorrected [$S^{1,3}$, Eq. (5)]. Column 2 (c,d) is ω_3-corrected [S^{1}, Eq. (10)]. Column 3 (e,f) is ω_1 and ω_3-corrected [S, Eq. (15)]. Column 4 (g,h) shows the real equilibrium 2D IR spectra of diglycine at 1 mg/mL (OD ~0.05). **g** is the equilibrium 20 °C spectrum. **h** shows the difference between the 30 and 20 °C equilibrium spectra. The spectra are individually normalized and scaled such that 25 linearly-spaced contours span the entire magnitude range of $\sinh(S_{\text{Norm.}} \times 0.1)$.

Because of the gradual nature of depletion of beams 1 and 2, the ω_1-correction factor is expected to be smaller than the ω_3-correction, which results from depletion of beam 3, the signal, and the LO over the entire length of the sample. The sharp features in Fig. 4(a) are the result of transient absorption due to the solute, while the broad baseline transient change is due to the solvent. Corrections for both the linear absorbance of the solute and solvent are necessary to reveal the underlying nonlinear signal.

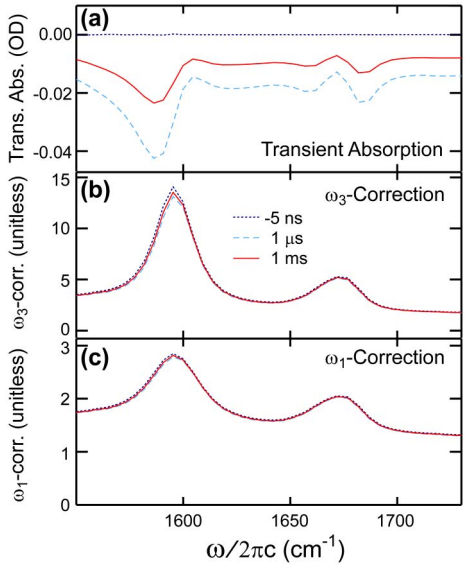

Fig. 4. (Color online) −5 ns, 1 μs, and 1 ms difference spectra for diglycine in D_2O. (a) The transient difference absorption spectra of diglycine and solvent calculated from the transient LO spectra $(-\log[I^{\circ}(\omega;\tau^{j})/I^{\circ}(\omega;\tau^{\text{ref}})])$. (b) The ω_3-correction factor, $\exp[2\kappa(\omega;\tau^{j})\omega l/c]$. **c** The ω_1-correction factor, $[K(\omega;\tau^{j})]^{-1}$.

Figures 3(g) and 3(h) show the 2D IR spectra from equilibrium experiments of diglycine at a much lower concentration of 1 mg/mL, where the effects of beam absorption by the solute should be negligible given the low ~0.05 OD of the diglycine. The equilibrium spectrum [Fig. 3(g)] is more similar to the ω_1- and ω_3-corrected spectrum than it is to the uncorrected spectrum, as is evident in the peak positions and lineshapes. The equilibrium carboxylate peak is weak because the beam spectrum was weaker on the red side on the day these data were collected. The 30 °C–20 °C equilibrium difference spectrum [Fig. 3(h)] is most similar to the ω_1- and ω_3-corrected transient difference spectrum, which suggests that the full correction returns the least distorted representation of the spectrum. Differences between the Figs. 3(h) and 3(f) spectra may be due to noise, slight phasing errors, uncorrected solvent transmission changes in Fig. 3(h), and possible deviations from linear response in the T-jump case. Because of the experimentally fixed relative phasing and back-to-back collection of the transient spectra, we find that collecting T-dependent data transiently provides better signal-to-noise than collecting in equilibrium.

To understand the effects of linear absorption correction on the HDVE spectra, projections of the 2D surfaces onto ω_3 are compared to DPP spectra obtained from HDVE measurements in Fig. 5. Theoretically, the projection of the absorptive (real) 2D spectrum onto ω_3 is equal to the DPP. There is good agreement between the 2D projections and DPP. This is particularly interesting in Figs. 5(e) and 5(f), where agreement indicates that the assumptions made for Eq. (16) are reasonable for this case, where diagonal features dominate the 2D spectrum. Just as in the case for the 2D surfaces, corrections to account for linear absorption cause significant changes in the difference spectra, where Fig. 5(b) only contains a few peaks compared to Figs. 5(d) and 5(f).

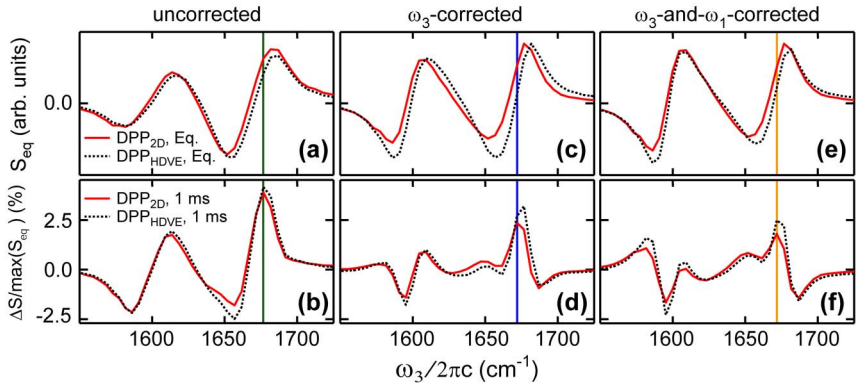

Fig. 5. (Color online) For 20 mg/mL diglycine, HDVE-derived DPP slices are compared to projections of the real 2D IR spectrum onto ω_3. Spectra are shown at equilibrium (first row) and at 1 ms delay time (second row). The three columns represent uncorrected (a,b), ω_3-corrected (c,d), and ω_3–and–ω_1–corrected (e,f) data analogous to the data shown in Fig. 3. The vertical lines indicate the maximum of the amide I' peak difference spectrum, whose traces are shown in Fig. 6.

Differences between Fig. 5(c) and 5(e) are less pronounced and again manifest themselves as reweighting of the carboxylate peaks.

Corrections for linear absorption are necessary for properly interpreting difference spectral features. As is shown in Fig. 6, the timescales observed in the DPP of diglycine change negligibly with correction because both the timescales of diglycine's T-jump response and the timescales of the transient absorption follow the temperature. The presence of spurious peaks in the uncorrected data, however, changes the molecular interpretation. Previous mid-IR T-jump experiments have not explicitly corrected for the linear transient absorption. Instead, previous work has attempted to differentiate between these transmission changes and temperature-induced sample changes by identifying temperature-dependent spectral features or time scale differences between the observed signal and the temperature's time profile [21,24,38]. We aim to correct for as much of the transient absorption distortions as possible using reasonable corrections to avoid having to differentiate the desired signal from the transient absorption effects.

C. Diglycine: Interpretation of Transient Results

Once the full correction is applied, the 'truest' transient and equilibrium spectra are given in Figs. 3(e) and 3(f). The carboxylate peak (lower left corner) of the ω_3- and ω_1-corrected difference spectrum [Fig. 3(f)] shows loss on the red side (marked with the vertical line) and a slight gain on the blue side. The amide I' peak difference spectrum (upper right corner) appears to be the result of two loss features (marked with vertical lines), but the observed doublet can be more consistently described by loss of the equilibrium peak and gain of a narrower center peak, which results in the low amplitude, broad off-diagonal gain intensity. The dominance of loss features over gain is consistent with the transient absorption spectrum and may be the result of non-Condon effects, like those observed in temperature-dependent FTIR studies of NMA [39,40] or shifting of oscillator strength to other coupled vibrational modes that lie outside of our spectral window.

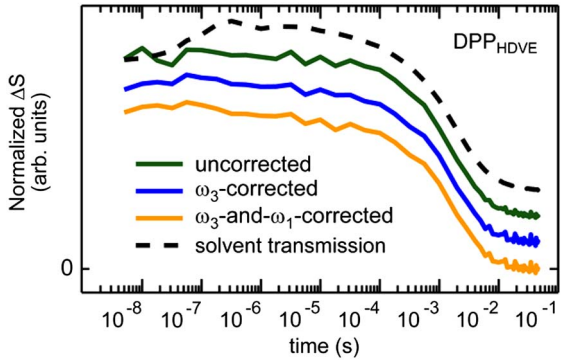

Fig. 6. (Color online) Slices taken from the DPP spectra shown in Fig. 5 at 1677, 1672, and 1672 cm^{-1}, respectively. Traces are offset to allow comparison. The dashed line shows the solvent transmission.

The time-dependence of frequency slices from the HDVE-derived DPP are shown in Fig. 6. Diglycine's spectral response tracks the solvent temperature profile, indicating that the observed changes happen on the sub-pulse-width limited, <10 ns time scale, which causes the 'immediate' jump away from equilibrium. Because of this fast reequilibration time, the diglycine sample is always equilibrated to the temperature of the solvent. The ~100 ns rise in the transient transmission spectrum shown in Fig. 6 is thought to be the result of cavitation in the sample [22]. This rise is largely removed from the nonlinear signal through linear absorption corrections.

Based on the fast response and the localized nature of the vibrations, we assign the difference peaks in Fig. 3(f) to a decrease in the average number of H-bonds. The addition of T-jump energy causes an increase in the magnitude of the fluctuations both in the solvent and in the peptide. These fluctuations decrease the average number of H-bonds and cause a slight blue-shift of the peak, which is observed as a loss on the red side and gain on the blue side. However, a simple frequency shift cannot describe all changes in the amide I' peak, such as the dominance of loss without equivalent gain in this spectral region. Because the amide I' frequency, linewidth, and transition dipole strength reflect the population of hydrogen bonding configurations, the inhomogeneous nature of the equilibrium peak indicates that there are multiple H-bonding configurations. The temperature change causes population to shift between these configurations and the resulting interference features result from the shifted frequency and decreased transition dipole as the average number of H-bonds is decreased at higher temperature. Previous work on NMA has indicated that T-dependent amide I' FTIR peak shifts are explained by electrostatic changes that can be linked to fewer H-bonds due to the increased kinetic energy [40]. We expect

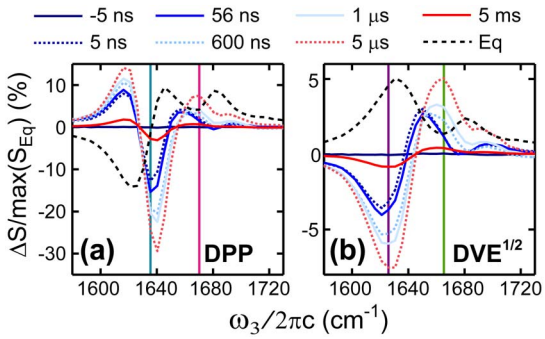

Fig. 7. (Color online) TZ2 transient spectra from t-HDVE measurements. (a,b) DPP and DVE spectra are shown at selected delays. The DVE spectra are actually presented as the square-root of the DVE power spectrum (the square-root is taken before subtraction gives the difference spectra) to remove the apparent factor of two rate of population change between the absolute-value-squared measurement and the DPP, which is linear in concentration [25].

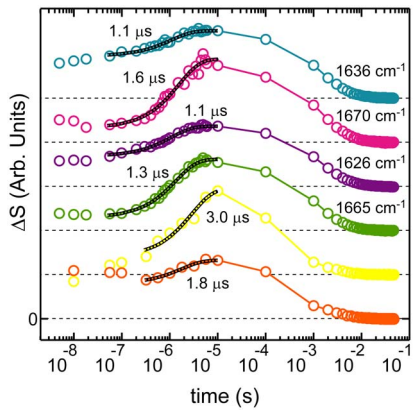

Fig. 8. (Color online) The TZ2 time-dependent trace and exponential fit. The top two traces are from the DPP [Fig. 7(a)], the middle two traces are from the square-root of the DVE [Fig. 7(b)], and the bottom two traces are from integrated boxes shown in Fig. 9(a).

similar changes for the amide I' peak of diglycine, although the terminal NH_3^+ group adds further sensitivity to the H-bonds at the N-terminus.

Regardless of the exact assignments, diglycine allows us to set a baseline for the simplest response that we can expect for a sample where we expect the primary response to T-jump to be picosecond solvation, including hydrogen bonding changes with the solvent. The t-2D IR also provides an explanation and a spectrum for the 'burst phase' signal that other transient experiments have observed [41]. For larger, more complicated peptides, we expect to see a similar pulse width limited response. Deviations from this T-jump tracking signal indicate conformational changes.

D. Trpzip2

The t-HDVE spectra of TZ2 are shown in Fig. 7. The t-HDVE data is displayed in two forms: as the real spectra (DPP) [Fig. 7(a)] and the absolute-value-squared DVE spectra [Fig. 7(b)]. Because of the presence of both negative and positive peaks, negative and positive features in the DPP difference spectrum can be the result of loss or gain. The DPP difference spectra show three major spectral features: a positive (loss compared to equilibrium) peak at 1612 cm^{-1}, a negative (loss) peak at 1636 cm^{-1}, and a positive (gain) feature that appears to shift with time from 1655 to 1670 cm^{-1}. The DVE difference spectra, whose equilibrium spectrum is entirely positive, have two major features: a negative (loss) feature that shifts from 1621 to 1626 cm^{-1} and a positive (gain) peak that shifts from 1650 to 1665 cm^{-1}. All three DPP and both DVE peaks are immediately present at 10 ns, grow in on the 1.1–1.6 μs time scale and then decay away following the temperature relaxation, as is shown by the normalized time traces in Fig. 8. The μs time scale is consistent with previous T-jump experiments on TZ2 [31,42]. We interpret the DPP 1612 and 1636 cm^{-1} and the DVE 1626 cm^{-1} loss features as loss of the most intense equilibrium spectrum feature, the peak at 1636 cm^{-1}. Shifting of the higher frequency peaks in both *difference* data representations indicates the appearance of at least two peaks, which is interpreted as evidence of at least two species that appear concomitant with loss of the equilibrium population; one species appears at <10 ns followed by at least one other on the 1–1.6 μs exponential time scale.

The real and absolute value t-2D IR spectra are shown in Fig. 9. The projection of the complex difference t-2D IR are equivalent to the complex 1D difference t-HDVE data, which means we can directly compare the DPP to the projection of the real t-2D IR onto the ω_3 axis. As with the t-HDVE data, there are changes in the t-2D IR at the earliest accessible times. The 56 and 100 ns difference t-2D IR are dominated by loss along the diagonal, in particular loss of the two peaks at 1636 and 1670 cm^{-1}, whose presence is indicative of antiparallel β-strand structure [43]. Aside from the loss, there are also two peaks indicating gain: the broad red/yellow peak above the diagonal and the blue ridge below the diagonal that extends along the $\omega_3 = 1636\ cm^{-1}$ horizontal line. These peaks are particularly clear in the absolute value difference spectra [Figs. 9(f) and 9(g)], where red (blue) is gain (loss). The loss and gain features are indicative of broadening into the antidiagonal, or homogeneous, dimension, which is consistent with increased flexibility and decreased numbers of H-bonds to the solvent, two effects that are expected with increased temperature. In the absence of our linear absorption corrections, contributions from direct solvent changes could not have been definitely ruled out of this assignment. As in the case with diglycine, we expect that these <10 ns changes in the spectrum are due to small amplitude conformational changes and response of the solvent interacting with the peptide, not large amplitude peptide motion. Although H-bonds across the backbone might be weakened, we do not expect that they are entirely lost.

Comparison of the 100 ns, 1 μs, and 5.6 μs spectra t-2D IR spectra reveals that peaks shift on the μs time scale. In the real t-2D IR spectra, the positive (gain) peak in the upper diagonal shifts up and increases in size and intensity, which causes the positive 1665 cm^{-1} peak in the DPP spectra. The negative (gain) ridge along $\omega_3 = 1636\ cm^{-1}$ also changes; it shifts up, broadens, and increases in intensity. These changes are reflected in the absolute value spectra where gain is stronger than loss along the diagonal in the 1660 cm^{-1} region at 5.6 μs. Based on the empirical correlations between amide I frequency and protein secondary structure [44], the appearance of intensity in the 1660 cm^{-1} region suggests an increase of disordered chains. Inspection of the integrated area shown in Fig. 9(a) (Fig. 8, bottom two traces) shows that peaks in the real t-2D IR also relax on the microsecond time scale,

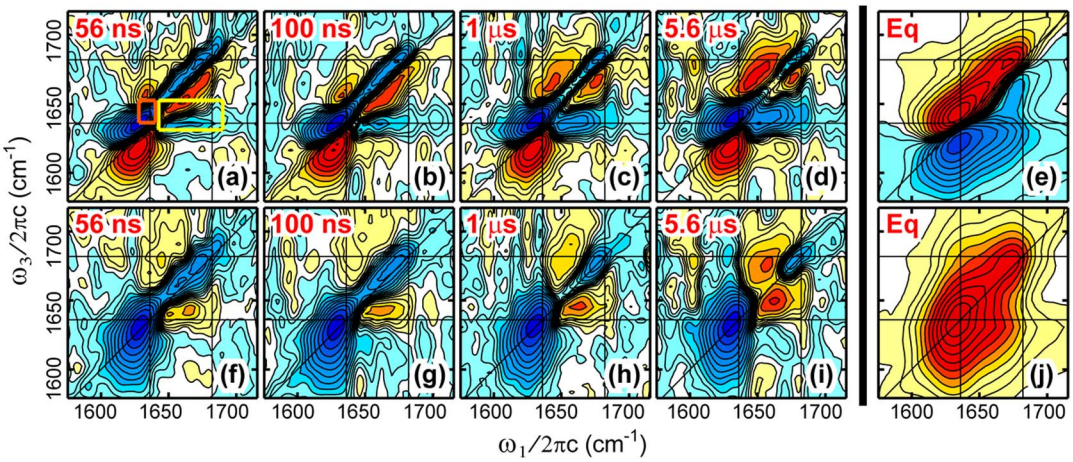

Fig. 9. (Color online) (a-e) The absorptive (real) correlation t-2D IR spectra at selected time delays for TZ2. (f-j) The t-2D IR square-root power spectra at selected time delays. The spectra are individually normalized and scaled such that 25 linearly-spaced contours span the entire magnitude range of $\sinh^{-1}(S_{\text{Norm.}} \times 27.29)$.

although the t-2D IR data is much noisier than the t-HDVE. The microsecond time scale is consistent with unfolding timescales and we attribute the changes in this time frame to loss of the native β-hairpin structure.

The t-HDVE and t-2D IR spectra and timescales can be explained by a three state kinetic model based on the presence of just two distinguishable time scales that are distinct from the thermal relaxation profile. Although there may be more states that are hidden within the noise, share the same spectral and temporal response as those described, or do not map well onto the H-bond sensitive amide I vibration, we can only distinguish relaxation rates of <10 ns and 1–1.6 μs. As in the case with diglycine, we hypothesize that the <10 ns response is due to H-bond changes resulting from increased local fluctuations due to the increased temperature, which causes a loss of the equilibrium spectrum and the gain of a broader, two peaked spectrum. On the μs time scale we see a shift in intensity to the 1660 cm^{-1} region, which indicates thermal disordering and unfolding of the backbone.

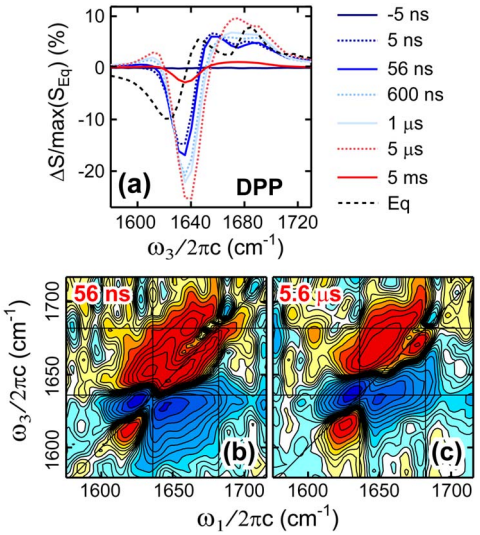

Fig. 10. (Color online) TZ2 uncorrected [$S^{1,3}$, Eq. (5)] difference DPP (a) and difference 2D IR (b,c) spectra, which can compared to the corrected data in Figs. 7(a), 9(a), and 9(d) . The 2D contours are plotted as described in Fig. 9.

Because of the low TZ2 concentration and ~0.05 OD, the majority of the transient linear absorption distortion is due to the solvent. The temperature profile is relatively flat during the 100 ns–10 μs time frame and the distorting linear absorption is not expected to significantly affect the observed relaxation time scales. The relaxation measured at 1636 and 1670 cm^{-1} from the uncorrected DPP can be fit to an exponential relaxation with time constants of 0.9 and 1.3 μs, which are similar to the 1.1 and 1.6 μs measured in the ω_3- and ω_1-corrected DPP traces shown in Fig. 8. The main differences between the corrected and uncorrected TZ2 data are in the spectra, not the time scales. The uncorrected TZ2 transient DPP and transient 2D IR spectra are shown in Fig. 10. In the uncorrected DPP, there are more intense changes on the blue side and less on the red side relative to the corrected DPP (Fig. 7). The uncorrected transient 2D IR spectra show additional strong red and blue peaks above and below the diagonal, respectively, which obscure the off-diagonal gain features as well as much of the diagonal loss features discussed above and shown in Fig. 9. As discussed before, the linear absorption distortions primarily add equilibrium spectral features into the transient spectra. This is consistent with the uncorrected DPP and 2D IR transient spectra, which appear to contain the undistorted features from Figs. 7 and 9 masked by broad equilibrium peak features. Although the observed time scales are the same within fitting error, the uncorrected spectra contain different peaks and different relative amplitudes which may have affected the spectral interpretation. Even in this case with a low OD solute, we find that the linear absorption correction is necessary to properly interpret the data.

5. CONCLUSION

Transient multidimensional spectroscopy is an attractive experimental technique which combines the rich information content of multidimensional spectroscopies with the ability to access arbitrarily long time scales. The increase in complexity inherent to transient experiments, however, makes it hard to both cleanly measure the desired signal and to interpret the results once collected. Through linear absorption corrections, we have shown a method for simplifying transient nonlinear spectra by removing distortions that can potentially

lead to false conclusions. These linear absorption corrections are general and can be applied to any transient 2D or DPP spectroscopy, including electronic spectroscopies, particularly in cases with a large transient absorption response. When applied to T-jump t-2D IR experiments on diglycine, these corrections reveal that amide I spectroscopy is sensitive to <10 ns changes in local H-bonds, a spectral signature that is relevant to all T-jump spectroscopies. When applied to the peptide TZ2, T-jump t-2D IR indicates at least three kinetic states: on the <10 ns time scale, H-bonds are lost and the β-hairpin begins to loosen and on the 1.1 μs time scale, the peptide disorders. The spectral analysis is enriched by the increased information content provided by t-2D IR spectroscopy. The combination of t-HDVE and t-2D IR spectroscopy provides both high time resolution and detailed spectra that allow us to interpret congested spectra.

ACKNOWLEDGMENTS

We thank Carlos Baiz and Andrew D. Horning for helpful comments. This work was supported by the National Science Foundation (NSF) (Grants CHE-0616575 and CHE-0911107).

REFERENCES

1. S. Woutersen and P. Hamm, "Structure determination of trialanine in water using polarization sensitive two-dimensional vibrational spectroscopy," J. Phys. Chem. B **104**, 11316–11320 (2000).
2. A. Remorino, I. V. Korendovych, Y. Wu, W. F. DeGrado, and R. M. Hochstrasser, "Residue-specific vibrational echoes yield 3D structures of a transmembrane helix dimer," Science **332**, 1206–1209 (2011).
3. C. J. Fecko, J. D. Eaves, J. J. Loparo, A. Tokmakoff, and P. L. Geissler, "Ultrafast hydrogen bond dynamics in the infrared spectroscopy of water," Science **301**, 1698–1702 (2003).
4. H. Ishikawa, K. Kwak, J. K. Chung, S. Kim, and M. D. Fayer, "Direct observation of fast protein conformational switching," Proc. Natl. Acad. Sci, U.S.A. **105**, 8619–8624 (2008).
5. J. F. Cahoon, K. R. Sawyer, J. P. Schlegel, and C. B. Harris, "Determining transition-state geometries in liquids using 2D-IR," Science **319**, 1820–1823 (2008).
6. J. R. Zheng, K. Kwak, J. Asbury, X. Chen, I. R. Piletic, and M. D. Fayer, "Ultrafast dynamics of solute-solvent complexation observed at thermal equilibrium in real time," Science **309**, 1338–1343 (2005).
7. Z. Ganim, H. S. Chung, A. W. Smith, L. P. DeFlores, K. C. Jones, and A. Tokmakoff, "Amide *I* two-dimensional infrared spectroscopy of proteins," Acc. Chem. Res. **41**, 432–441 (2008).
8. A. T. Krummel, P. Mukherjee, and M. T. Zanni, "Inter and intrastrand vibrational coupling in DNA studied with heterodyned 2D-IR spectroscopy," J. Phys. Chem. B **107**, 9165–9169 (2003).
9. T. Brixner, J. Stenger, H. M. Vaswani, M. Cho, R. E. Blankenship, and G. R. Fleming, "Two-dimensional spectroscopy of electronic couplings in photosynthesis," Nature **434**, 625–628 (2005).
10. M. Khalil, N. Demirdoven, and A. Tokmakoff, "Coherent 2D IR spectroscopy: molecular structure and dynamics in solution," J. Phys. Chem. A **107**, 5258–5279 (2003).
11. M. D. Fayer, "Dynamics of liquids, molecules, and proteins measured with ultrafast 2D IR vibrational echo chemical exchange spectroscopy," Annu. Rev. Phys. Chem. **60**, 21–38 (2009).
12. J. N. Bandaria, S. Dutta, M. W. Nydegger, W. Rock, A. Kohen, and C. M. Cheatum, "Characterizing the dynamics of functionally relevant complexes of formate dehydrogenase," Proc. Natl. Acad. Sci, U.S.A. **107**, 17974–17979 (2010).
13. C. Fang, J. D. Bauman, K. Das, A. Remorino, E. Arnold, and R. M. Hochstrasser, "Two-dimensional infrared spectra reveal relaxation of the nonnucleoside inhibitor TMC278 complexed with HIV-1 reverse transcriptase," Proc. Natl. Acad. Sci, U.S.A. **105**, 1472–1477 (2008).
14. J. M. Anna, M. R. Ross, and K. J. Kubarych, "Dissecting enthalpic and entropic barriers to ultrafast equilibrium isomerization of a flexible molecule using 2DIR chemical exchange spectroscopy," J. Phys. Chem. A **113**, 6544–6547 (2009).
15. J. Bredenbeck, J. Helbing, R. Behrendt, C. Renner, L. Moroder, J. Wachtveitl, and P. Hamm, "Transient 2D-IR spectroscopy: snapshots of the nonequilibrium ensemble during the picosecond conformational transition of a small peptide.," J. Phys. Chem. B **107**, 8654–8660 (2003).
16. J. Bredenbeck, J. Helbing, and P. Hamm, "Labeling vibrations by light: ultrafast transient 2D-IR spectroscopy tracks vibrational modes during photoinduced charge transfer," J. Am. Chem. Soc. **126**, 990–991 (2004).
17. C. Kolano, J. Helbing, M. Kozinski, W. Sander, and P. Hamm, "Watching hydrogen-bond dynamics in a β-turn by transient two-dimensional infrared spectroscopy," Nature **444**, 469–472 (2006).
18. R. Kania, A. I. Stewart, I. P. Clark, G. M. Greetham, A. W. Parker, M. Towrie, and N. T. Hunt, "Investigating the vibrational dynamics of a 17e- metallocarbonyl intermediate using ultrafast two dimensional infrared spectroscopy," Phys. Chem. Chem. Phys. **12**, 1051–1063 (2010).
19. C. R. Baiz, M. J. Nee, R. McCanne, and K. J. Kubarych, "Ultrafast nonequilibrium Fourier-transform two-dimensional infrared spectroscopy," Opt. Lett. **33**, 2533–2535 (2008).
20. W. Xiong, J. E. Laaser, P. Paoprasert, R. A. Franking, R. J. Hamers, P. Gopalan, and M. T. Zanni, "Transient 2D IR spectroscopy of charge injection in dye-sensitized nanocrystalline thin films," J. Am. Chem. Soc. **131**, 18040–18041 (2009).
21. H. S. Chung, Z. Ganim, K. C. Jones, and A. Tokmakoff, "Transient 2D IR spectroscopy of ubiquitin unfolding dynamics," Proc. Natl. Acad. Sci, U.S.A. **104**, 14237–14242 (2007).
22. H. S. Chung, M. Khalil, A. W. Smith, and A. Tokmakoff, "Transient two-dimensional IR spectrometer for probing nanosecond temperature-jump kinetics," Rev. Sci. Instrum. **78**, 063101 (2007).
23. E. R. Andresen and P. Hamm, "Site-specific difference 2D-IR spectroscopy of Bacteriorhodopsin," J. Phys. Chem. B **113**, 6520–6527 (2009).
24. H. S. Chung, M. Khalil, A. W. Smith, Z. Ganim, and A. Tokmakoff, "Conformational changes during the nanosecond to millisecond unfolding of ubiquitin," Proc. Natl. Acad. Sci. USA **102**, 612–617 (2005).
25. C. R. Baiz, R. McCanne, and K. J. Kubarych, "Transient vibrational echo versus transient absorption spectroscopy: a direct experimental and theoretical comparison," Appl. Spectrosc. **64**, 1037–1044 (2010).
26. K. C. Jones, Z. Ganim, and A. Tokmakoff, "Heterodyne-detected dispersed vibrational echo spectroscopy," J. Phys. Chem. A **113**, 14060–14066 (2009).
27. Although the transient absorption signal is formally 3rd order, here we take a phenomenological approach in which the *T*-jump pulse is not considered in the nonlinear spectral response.
28. J. Wang and M. A. El-Sayed, "Temperature jump-induced secondary structural change of the membrane protein bacteriorhodopsin in the premelting temperature region: a nanosecond time-resolved fourier transform infrared study," Biophys. J. **76**, 2777–2783 (1999).
29. S. Williams, T. P. Causgrove, R. Gilmanshin, K. S. Fang, R. H. Callender, W. H. Woodruff, and R. B. Dyer, "Fast events in protein folding: helix melting and formation in a small peptide," Biochemistry **35**, 691–697 (1996).
30. C.-Y. Huang, J. W. Klemke, Z. Getahun, W. F. DeGrado, and F. Gai, "Temperature-dependent helix-coil transition of an alanine based peptide," J. Am. Chem. Soc. **123**, 9235–9238 (2001).
31. K. Hauser, C. Krejtschi, R. Huang, L. Wu, and T. A. Keiderling, "Site-specific relaxation kinetics of a tryptophan zipper hairpin peptide using temperature-jump IR spectroscopy and isotopic labeling," J. Am. Chem. Soc. **130**, 2984–2992 (2008).
32. H. Ma, J. Ervin, and M. Gruebele, "Single-sweep detection of relaxation kinetics by submicrosecond midinfrared spectroscopy," Rev. Sci. Instrum. **75**, 486–491 (2004).
33. A. W. Smith, J. Lessing, Z. Ganim, C. S. Peng, A. Tokmakoff, S. Roy, T. L. C. Jansen, and J. Knoester, "Melting of a β-hairpin peptide using isotope-edited 2D IR spectroscopy and simulations," J. Phys. Chem. B **114**, 10913–10924 (2010).

34. J. D. Hybl, A. Albrecht Ferro, and D. M. Jonas, "Two-dimensional fourier transform electronic spectroscopy," J. Chem. Phys. **115**, 6606–6622 (2001).
35. N. Belabas and D. M. Jonas, "Three-dimensional view of signal propagation in femtosecond four-wave mixing with application to the boxcars geometry," J. Opt. Soc. Am. B **22**, 655–674 (2005).
36. M. K. Yetzbacher, N. Belabas, K. A. Kitney, and D. M. Jonas, "Propagation, beam geometry, and detection distortions of peak shapes in two-dimensional Fourier transform spectra," J. Chem. Phys. **126**, 044511 (2007).
37. S. Ham, J.-H. Kim, H. Lee, and M. Cho, "Correlation between electronic and molecular structure distortions and vibrational properties. II. amide I modes of NMA-nD2O complexes," J. Chem. Phys. **118**, 3491–3498 (2003).
38. Adam W. Smith and A. Tokmakoff, "Probing local structural events in β-hairpin unfolding with transient nonlinear infrared spectroscopy," Angew. Chem.. Int. Ed. Engl., Suppl. **46**, 7984–7987 (2007).
39. K. E. Amunson and J. Kubelka, "On the temperature dependence of amide I frequencies of peptides in solution," J. Phys. Chem. B **111**, 9993–9998 (2007).
40. J. Kaminsky, P. Bour, and J. Kubelka, "Simulations of the temperature dependence of the amide I vibration," J. Phys. Chem. A **115**, 30–34 (2011).
41. R. M. Ballew, J. Sabelko, and M. Gruebele, "Direct observation of fast protein folding: the initial collapse of apomyoglobin," Proc. Natl. Acad. Sci. U.S.A. **93**, 5759–5764 (1996).
42. C. D. Snow, L. Qiu, D. Du, F. Gai, S. J. Hagen, and V. S. Pande, "Trp zipper folding kinetics by molecular dynamics and temperature-jump spectroscopy," Proc. Natl. Acad. Sci. USA **101**, 4077–4082 (2004).
43. N. Demirdöven, C. M. Cheatum, H. S. Chung, M. Khalil, J. Knoester, and A. Tokmakoff, "Two-dimensional infrared spectroscopy of antiparallel β-sheet secondary structure," J. Am. Chem. Soc. **126**, 7981–7990 (2004).
44. A. Barth and C. Zscherp, "What vibrations tell us about proteins," Q. Rev. Biophys. **35**, 369–430 (2002).